

Disentangled Implicit Shape and Pose Learning for Scalable 6D Pose Estimation

Yilin Wen¹, Xiangyu Li², Hao Pan³, Lei Yang¹, Zheng Wang^{1,4}, Taku Komura¹, Wenping Wang¹

¹The University of Hong Kong ²Brown University ³Microsoft Research Asia ⁴SUSTech
 ylwen@hku.hk xiangyu.li@alumni.brown.edu haopan@microsoft.com
 lyang@cs.hku.hk wangz@sustech.edu.cn {taku, wenping}@cs.hku.hk

Abstract

6D pose estimation of rigid objects from a single RGB image has seen tremendous improvements recently by using deep learning to combat complex real-world variations, but a majority of methods build models on the per-object level, failing to scale to multiple objects simultaneously. In this paper, we present a novel approach for scalable 6D pose estimation, by self-supervised learning on synthetic data of multiple objects using a single autoencoder. To handle multiple objects and generalize to unseen objects, we disentangle the latent object shape and pose representations, so that the latent shape space models shape similarities, and the latent pose code is used for rotation retrieval by comparison with canonical rotations. To encourage shape space construction, we apply contrastive metric learning and enable the processing of unseen objects by referring to similar training objects. The different symmetries across objects induce inconsistent latent pose spaces, which we capture with a conditioned block producing shape-dependent pose codebooks by re-entangling shape and pose representations. We test our method on two multi-object benchmarks with real data, T-LESS and NOCS REAL275, and show it outperforms existing RGB-based methods in terms of pose estimation accuracy and generalization.

1. Introduction

Pose estimation of rigid objects from a single RGB image is a fundamental but challenging task in fields such as robotics and scene understanding, for which many efficient learning based methods have been developed recently [36, 50, 23]. A common limitation with many of these works is that a specialized network must be trained for each object, which makes it expensive to process multiple objects by switching and streaming to specific networks, and renders it impossible to handle novel objects without re-training the network.

This work was done when Yilin Wen and Xiangyu Li were interns at Microsoft Research Asia

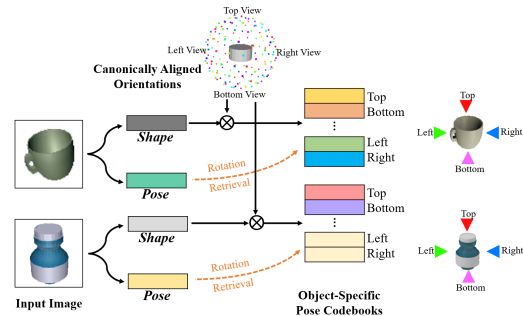


Figure 1: Images of objects are mapped into latent representations for object shape and pose, respectively. Due to different symmetries of objects, the canonically aligned orientations must be re-entangled with the object shape to generate the object-specific pose codebooks (symmetries marked by code color), against which the latent pose codes are compared to retrieve the object rotations.

Key to the scalable pose estimation problem is the modeling of shape similarities among multiple objects, such that different objects can be aligned consistently into a single pose estimation model and a novel object can be processed by referring to training objects that have similar shapes to it. Previous methods approach this target in different ways. For example, Wang *et al.* [47] perform category-level pose estimation by mapping all instances of an object category to a normalized object coordinate space (NOCS) where the instances are consistently aligned, and predict for an input image the aligned NOCS shape which is registered with the input depth to obtain the 6D pose. Subsequent works [8, 43] improve the shape representation by focusing on detailed variance across instances. However, relying on the strong intra-category geometric consistency prevents these methods from handling very different objects across categories. On the other hand, Multipath-AAE [38] makes no intra-category consistency assumption and proposes to accommodate different instances by using a specific decoder for each instance to reconstruct images in an auto-encoding fashion, which, however, has limited scalability as the number of training objects increases.

We address the scalability issue of object pose estimation by encoding objects of arbitrary classes into implicit codes using a common auto-encoder. Given an input image bounding the object of interest, we train the auto-encoder to *disentangle* the object shape and pose by mapping the image to their respective latent spaces before reconstruction; therefore, at test stage, the latent pose code can be compared with a pose codebook indexed by canonically aligned rotations for retrieval of the object rotation (see Figs. 1, 2 for an illustration).

While the pipeline seems trivially applicable to many objects, the variation in symmetries of objects makes it impossible to generate a pose codebook for all kind of objects from canonically aligned rotations only. For example, the cup in Fig. 1 has distinctive codes for representing the left and right views, but the rotational symmetry of the bottle demands an identical code for the two views. This exemplifies the frequent infeasibility of disentangling an input image into *independent* latent factors by a neural network [3], the factors being shape and pose in our case.

To cope with this problem, we model the shape-pose dependency by introducing a conditioned block that *re-entangles* the shape and rotation information and generates an object-conditioned pose codebook, against which the query latent pose code is compared for pose retrieval. In addition, to facilitate generalization to novel objects, we take advantage of the separated latent shape space and apply contrastive metric learning, which encourages objects with similar geometry to have similar shape codes. By training the system with diverse shapes and categories, unseen objects can be robustly processed by referring to similar training objects with proximate latent shape codes.

Our technical contribution in this paper for solving the 6D pose estimation problem can be summarized as follows:

- (1) disentanglement of shape and pose to enhance the scalability of the pose prediction to a wide range of object shapes and classes;
- (2) re-entanglement of shape and pose, which makes the pose space conditioned on object shape to respect the particular symmetry of each object instance;
- (3) learning the metric shape space by a contrastive prior, so that the similarity of objects with diverse shapes and semantic categories can be captured and leveraged for generalizing to unseen objects.

We evaluate our method by training our system on synthetic data only and testing it on real data. We consider two settings: the first assumes the novel test objects are from known categories but without 3D models [47, 43, 8], and the other assumes we have the 3D models of the test objects but without categorical shape consistency with training objects [38]. To the best of our knowledge, this is the first time the two settings are processed by one framework. We compare the proposed method with existing baselines

on two most commonly used benchmarks, REAL275 [47] and T-LESS [19]. We also validate our design choices with extensive ablation studies. The results justify the proposed designs and show the gains in accuracy and generalization with respect to existing RGB-based methods.

2. Related Works

6D Pose estimation There is a massive literature of instance-level pose estimation from RGB(D) images (we refer the readers to [26] for a comprehensive survey), which can be roughly classified into three streams, *i.e.*, by direct pose regression [50, 23, 2], by registering 2D and 3D points [4, 36, 41, 33, 31], and by template retrieval [18, 39, 40, 51, 48]. Most learning based methods train specialized networks for testing instances.

Wang *et al.* [47] propose a shared shape representation of all instances in a category, which aligns and normalizes the objects into a common unit cubic volume. It is expected that variations among the instances are smooth and therefore predictable in the NOCS space, which is learned by training on large scale categorical datasets like ShapeNet [5]. For pose estimation, the pixels of a detected object are mapped to surface points in the NOCS space, which are registered with the input depth image to find the 6D rigid transformation along with scaling. Grabner *et al.* [12] use a similar canonical object coordinate representation for category level 3D model retrieval.

Subsequent works improve on the NOCS pipeline by focusing on modeling the shape differences. Chen *et al.* [6] propose to learn an implicit encoding space of instance shape variations by training a VAE, which is concatenated with another encoding of the input RGBD data to predict the 6D pose. Tian *et al.* [43] first learn the shape space of an object category by a point cloud autoencoder, and then compute a point cloud that represents a mean shape by decoding the mean code. The pose is estimated by adaptively deforming the mean shape and registering it to the input depth map. Chen *et al.* [8] similarly train a VAE for shape encoding, and synthesize the 2D appearance of an object under a given pose by neural rendering conditioned on both the shape code and the pose transformation; during test time, both the object shape code and its pose transformation are searched by gradient descent to match the neural rendered image with the observation. These works rely on the intra-category shape consistency and have difficulty processing multiple categories with drastic shape variances.

Multipath-AAE [38] works under a different assumption where the 3D models of test objects are available, which is common for settings like manufacturing. It extends the augmented autoencoder approach [40] to multiple objects by sharing an encoder and assigning to each object an individual decoder, which bypasses the shape difference problem. Its encoder can learn pose-aware features that generalize to different objects. Similarly, Pitteri *et al.* [34] use learned lo-

cal surface embedding to estimate pose for unseen objects with given 3D test models.

Our direct approach disentangles the input image into separated shape and pose representations, where the pose code can be compared with canonical rotations for pose estimation, and the metric shape space facilitates novel object processing. Compared with [38], our disentanglement saves the cost of accommodating multiple objects with their respective decoders, although the disentanglement is nontrivial and requires the shape conditioned pose codebook generation. Unlike [43, 8], our latent shape space is learned with contrastive learning and extensible to diverse objects across categories. In addition, our framework enables the seamless processing of the two settings used previously (*i.e.*, with or without test 3D models) for the first time in literature.

Disentangled representation learning Disentanglement is identified as a key objective for learning representations that are interpretable and generalized [1, 28]. Works have been proposed to encourage disentangled representation learning by unsupervised learning [16, 9]. Recently, focus has been given to the conditions under which learned representations can be disentangled [29, 15, 24], with the finding that quite frequently the direct mapping to disentangled independent factors are unattainable for neural networks [3]. Our discussion on the multi-object 6D pose estimation exemplifies the situation: the disentanglement of object shape and pose as independent factors are prevented by different object symmetries. We provide a solution to the disentanglement problem by re-entangling the independent factors so that a neural network mapping becomes learnable.

3. Method

Our overall framework is an autoencoder that learns to encode observed objects to their latent shape and pose codes. During test stage, it compares the latent pose code with a codebook of implicit rotation representations for fast pose estimation. To be specific, we have an encoder E that maps an input RGB image containing the object to a latent representation with two parts, z_o and z_p , that encode the object shape and object-dependent pose, respectively. The two latent codes are fed into the decoder network D^{rgb} to recover the original input image. The decoder can be extended with an additional branch D^{depth} for depth map reconstruction that can be used for translation estimation given the depth signal at test time (Sec. 4.1). The whole network is shown in Fig. 2. Notably, our framework differs from the typical auto-encoding pipeline in modeling the similarity of different object shapes and in the entangling of object shape with pose code generation to produce the conditioned codebook for test time pose retrieval. Next we discuss the key designs in detail.

3.1. Disentangled shape and pose learning by auto-encoding

Given the input RGB image $\mathbf{I}_{o,p} \in \mathbb{R}^{3 \times H \times W}$ for an object o under pose $p \in \text{SE}(3)$, the encoder E maps $\mathbf{I}_{o,p}$ to a low-dimensional latent code $E(\mathbf{I}_{o,p}) = (z_o, z_p) \in \mathbb{R}^{2d}$ with $d \ll H \times W$, where $z_o, z_p \in \mathbb{R}^d$ encode the implicit shape and pose representations, respectively.

The decoder tries to recover the input image \mathbf{I} , given the latent codes. Since we expect the object shape code z_o to encode the overall object appearance and the pose code z_p to encode the view-specific appearance, we borrow ideas from generative models [10, 21, 22] and use the AdaIN modulation to condition the per-view image reconstruction on the object code in the decoder, as illustrated in Fig. 2. Specifically, we use the transformed shape information $(g_i^s, g_i^b) = FC_i(z_o) \in \mathbb{R}^{2C_i}$ to modulate the i -th intermediate feature map $\mathbf{F}_i \in \mathbb{R}^{C_i \times H_i \times W_i}$ decoded from the pose code, by

$$\tilde{\mathbf{F}}_i = g_i^s \odot \frac{\mathbf{F}_i - \mu(\mathbf{F}_i)}{\sigma(\mathbf{F}_i)} + g_i^b,$$

where FC_i is a fully connected layer; \odot is the element-wise product; and $\mu(\cdot)$ and $\sigma(\cdot)$ compute the mean and standard deviation vectors across the spatial dimensions, respectively.

Since we use only synthetic data for training, to narrow the domain gap between synthetic and real data, we follow [38, 39] and adopt data augmentations that randomly change the color and scaling of an input image \mathbf{I} to obtain the augmented image $\bar{\mathbf{I}}$, while aiming to recover the canonical image \mathbf{I} by auto-encoding. Thus to summarize, the loss function of the auto-encoding task is,

$$L_{recon} = \sum_{o,p} \|\mathbf{I}_{o,p} - D^{rgb}(E(\bar{\mathbf{I}}_{o,p}))\|^2. \quad (1)$$

Note that our design accommodates different objects by sharing the same set of trainable variables for E and D^{rgb} , and hence is different from [38] that assigns to each object an individual decoder and numerous previous works [48, 39] that train a specialized network for each object.

3.2. Contrastive metric learning for object shapes

Key to the generalization to novel objects is to exploit their similarities with known training objects. Therefore, we aim to build a metric space for the shape representations of training objects \mathcal{O} , spanned by $\{z_o\}_{o \in \mathcal{O}}$, such that similar shapes would have closer latent codes than different shapes. Given an unknown object at test time, its shape representation in the metric space thus refers to the symmetries of similar training objects when used for generating its specific pose space for pose estimation. We achieve this target by the contrastive metric learning [49, 45, 13, 7].

Denote the training object set as $\mathcal{O} = \{o_i\}_{i \in [N_O]}$, where N_O is the number of training objects. Similar to [49], to learn the contrastive metric among shape representations,

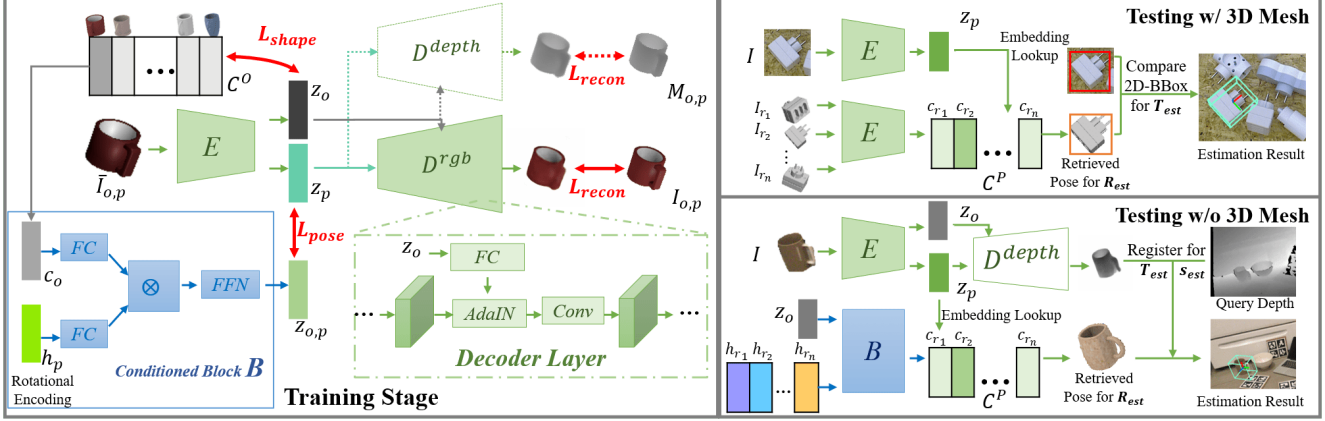


Figure 2: Illustration of our framework at the training stage and testing scenarios. Depending on whether the 3D model of the testing object is provided (Sec. 4.2) or not (Sec. 4.1), we construct a pose codebook \mathcal{C}^P accordingly and perform RGB-based rotation estimation by looking up in \mathcal{C}^P . When the 3D model of the testing object is unavailable, we use the depth decoder D^{depth} to estimate the translation; otherwise, we use the pinhole camera model for the same purpose.

we establish a shape embedding $\mathcal{C}^O \in \mathbb{R}^{N_o \times d}$ containing codes $\{\mathbf{c}_i \in \mathbb{R}^d\}_{i \in [N_o]}$ each of which corresponds to a training object. We then define the proximity of each \mathbf{c}_i to \mathbf{z}_o in the form of probability distribution as

$$\Pr(\mathbf{c}_i | \mathbf{z}_o) = \frac{\exp(\hat{\mathbf{c}}_i \cdot \hat{\mathbf{z}}_o / \tau)}{\sum_{j=1}^N \exp(\hat{\mathbf{c}}_j \cdot \hat{\mathbf{z}}_o / \tau)} \quad (2)$$

where τ is the temperature parameter to control the sharpness of the distribution, and $\hat{\mathbf{a}} = \frac{\mathbf{a}}{\|\mathbf{a}\|}$ denotes normalized unit-length vectors.

The target distribution given o is simply a one-hot vector $\mathbf{w}^o \in \{0, 1\}^{N_o}$, with $w_i^o = 1$ if $o = o_i$ and the rest entries being zero. The contrastive metric loss for modeling the shape space is then defined as

$$L_{shape} = - \sum_{o,p} \sum_{i=1}^{N_o} w_i^o \log \Pr(\mathbf{c}_i | \mathbf{z}_o). \quad (3)$$

To minimize the above loss, while \mathbf{z}_o is updated by SGD solver during each training step, we update the shape embedding \mathcal{C}^O by the exponential moving average (EMA) with decay rate d_s , thus making \mathbf{c}_o a smoothed history of \mathbf{z}_o . Details of the EMA update can be found in the supplementary document. During training, \mathbf{c}_o instead of \mathbf{z}_o is used for the conditioned pose generation (Sec. 3.3), which is shown to stabilize the training process. At test stage, however, we discard \mathcal{C}^O and use the learned \mathbf{z}_o to condition the pose codebook generation for a novel test object.

3.3. Re-entanglement of shape and pose

The pose code \mathbf{z}_p is compared with encodings of a sampled reference orientation space to retrieve the rotation of the object. As noted before (Fig. 1), different symmetries of objects demand the generation of object-specific pose codebooks. To enable such conditioned generation, we present a distributed representation of the rotations and the transformation that maps the rotations to implicit codes by entangling with shape in a generalizable way.

Rotational position encoding We need to distinguish between different rotations in a canonical pose representation. Inspired by the positional encoding in sequence models [46], we have adopted the 4D hyper spherical harmonics (HSH) rotation encoding. The HSH is the set of orthogonal basis functions on the 4D hypersphere that mimic the sine/cosine wave functions for positional encoding in sequence models: it is a distributed vector representation that can extend to high dimensions ($d = 128$ in our case), has a multi-spectrum structure that encodes both high frequency and low frequency variations of rotations, and has periodic structures with fixed linear transformations for relative rotations [52, 32]. Denoting the HSH function as $Z_{nl}^m(\beta, \theta, \phi)$, with $\beta \in [0, 2\pi]$, $\theta \in [0, \pi]$, $\phi \in [0, 2\pi]$ as the in-plane rotation, zenith and azimuth angles respectively for the rotation p and l, m, n as the polynomial degrees, we obtain the 128-dim vector encoding \mathbf{h}_p by ranging over $n \in [0, \dots, 6]$ with $0 \leq l \leq n, 0 \leq m \leq l$. Details of the construction can be found in the supplemental document.

Conditioned pose code generation As illustrated in Fig. 2, we design a conditional block B to entangle the object code \mathbf{c}_o with the rotational position encoding \mathbf{h}_p of rotation p and output a pose code $\mathbf{z}_{o,p} = B(\mathbf{c}_o, \mathbf{h}_p)$ comparable with \mathbf{z}_p .

Entanglement is a recurring topic in machine learning, with implementation techniques like parameter generation [35, 44, 10] that boil down to a tensor product structure [42, 30]. In particular, we introduce a 3rd-order learnable tensor $\mathbf{W} \in \mathbb{R}^{d \times d \times d}$ and apply the following two-step transformation B to obtaining the entangled pose code:

$$\begin{aligned} \mathbf{z}'_{o,p} &= \mathbf{W} (FC(sg(\mathbf{c}_o)), FC(\mathbf{h}_p)), \\ \mathbf{z}_{o,p} &= \text{FFN}(\mathbf{z}'_{o,p}), \end{aligned} \quad (4)$$

where $FC(sg(\mathbf{c}_o)), FC(\mathbf{h}_p) \in \mathbb{R}^d$ are the pre-processing of \mathbf{c}_o and \mathbf{h}_p , $sg(\cdot)$ is to stop gradient back-propagation, as

we expect c_o to be updated by z_o (Sec. 3.2), and $\mathbf{W}(\cdot, \cdot)$ denotes the tensor contraction along its first two ranks. We also introduce a feed-forward residual block FFN following the bilinear transform for post-processing, to generate the final pose code as $z_{o,p}$ for the object o under pose p .

Finally, to synchronize the pose representation computed via the conditioned block B with that learned by the encoder E , we minimize the cosine distance between $z_{o,p}$ and \hat{z}_p during the training stage:

$$L_{pose} = - \sum_{o,p} \hat{z}_{o,p} \cdot \hat{z}_p. \quad (5)$$

In summary, our total training loss combines the reconstruction loss (Eq. 1), the contrastive loss for shape representation learning (Eq. 3) and the synchronization loss to match the pose representations from B and E (Eq. 5), with two hyperparameter λ_1, λ_2 to weight different terms:

$$L = L_{recon} + \lambda_1 L_{shape} + \lambda_2 L_{pose}.$$

4. Inference under Different Settings

Our rotation estimation at the inference stage follows three steps (Fig. 2): Given the query RGB image crop \mathbf{I} bounding the object of interest, we first obtain its latent shape and pose codes as $(z_o, z_p) = E(\mathbf{I})$, then build a pose embedding codebook $\mathcal{C}^P \in \mathbb{R}^{N_P \times d}$ with each row $c_q \in \mathbb{R}^d$ corresponding to the rotation q from a set of N_P reference rotations $\mathcal{R} \subset SO(3)$, and finally retrieve the estimated pose as $q^* = \arg \max_{q \in \mathcal{R}} \hat{z}_p \cdot \hat{c}_q$. The translation estimation and possible scale estimation are done subsequently.

We note that previous works on multiple object pose estimation have assumed different testing scenarios, which we categorize into two common settings and build the pose embedding codebook \mathcal{C}^P correspondingly in order to follow and compare with previous works focusing on the different settings. The versatility of our framework is demonstrated through the application to different settings.

4.1. Objects with unknown 3D models of a known category

Following the series of NOCS related works [47, 8, 43], the 6D pose estimation is carried out for novel testing objects from a specific category whose 3D models are not available. In this setting, we use the conditioned block B to compute \mathcal{C}^P from the sampled reference rotations \mathcal{R} and the shape representation z_o , i.e. $\mathcal{C}^P = \{B(z_o, h_q)\}_{q \in \mathcal{R}}$.

While the orientation estimation is purely based on the RGB image, the translation estimation, however, becomes infeasible without the depth map due to the scale ambiguity of the novel object. To resolve this problem, we train the autoencoder with an extra depth branch D^{depth} to reconstruct a corresponding canonical depth map $D^{depth}(E(\bar{\mathbf{I}}_{o,p})) \in \mathbb{R}^{1 \times H \times W}$ given the input image. During test stage, we obtain the predicted depth map and align it with the query depth map to estimate the relative scaling and translation by

a rough comparison of the 3D bounding boxes and a further refinement with ICP [37].

To train the depth prediction branch, we extend the reconstruction loss Eq. (1) by adding another supervision with the groundtruth depth $\mathbf{M}_{o,p}$ on the depth reconstruction:

$$L_{recon} = \sum_{o,p} \|\mathbf{I}_{o,p} - D^{rgb}(E(\bar{\mathbf{I}}_{o,p}))\|^2 + \|\mathbf{M}_{o,p} - D^{depth}(E(\bar{\mathbf{I}}_{o,p}))\|^2. \quad (6)$$

Cross category pose estimation We further extend the NOCS setting and combine objects from all categories into one set, and challenge our method on this task that has never been addressed before. Previous methods have difficulty with this setting, as the drastic shape variances across categories violate the consistency assumption [47, 8, 43]. In contrast, our shape space metric learning (Sec. 3.2) is based on the object-level discrimination, which scales to more objects without the category limitation and enables robust generalization in this setting (Sec. 5.2).

4.2. Objects with known 3D model

In industrial settings like manufacturing, 3D CAD models of novel testing objects are usually known as assumed by [38, 34]. In this setting, we follow the previous works and render synthetic images \mathbf{I}_q of the given object under the reference orientations q , and map \mathbf{I}_q via encoder E to construct the offline pose codebook $\mathcal{C}^P = \{z_q\}_{q \in \mathcal{R}}$, with z_q obtained as the second part of $E(\mathbf{I}_q)$.

As the 3D CAD models have specific physical sizes, with known camera intrinsics we use the pinhole camera model for translation estimation from a single RGB image [38, 40]. The decoder network is not used for pose estimation.

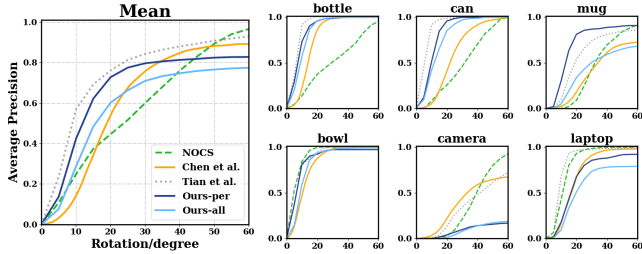
Through experiments (Sec. 5), we show that the trained encoder builds highly discriminative pose codebooks that perform even better than per-object trained networks and generalize to unseen objects with largely different shapes.

5. Experiments

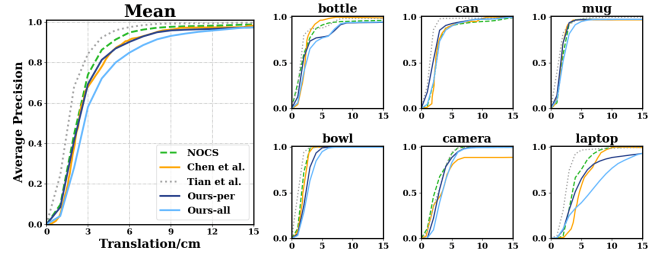
We evaluate our method on two widely used benchmarks for multiple-object 6D pose estimation, the NOCS dataset with unknown test object models [47] and the T-LESS dataset with known models [19]. Comparison with state-of-the-art works under the two scenarios are presented in Secs. 5.2 and 5.3. Ablation study on key design choices is conducted in Sec. 5.4.

5.1. Setup

We resize the input images to $H \times W = 128 \times 128$ and use latent code dimension $d=128$. We set $\lambda_1=0.004, \lambda_2=0.002$ to balance the different loss terms, and $\tau=0.07$ and $d_s=0.9999$ for EMA update in the shape contrastive metric learning. We use the Adam optimizer [25] with the learning rate as 0.0002, and train 50k iterations with a batch size of 64. To narrow down the domain gap between synthetic and real images, we perform data augmentation following [38]; details are provided in the supplementary document.



(a) **Rotation:** AP at different rotation error thresholds



(b) **Translation:** AP at different translation error thresholds

Figure 3: Comparison on REAL275. Reported are the average precisions under different rotation or translation error thresholds. We evaluate our method on both the per-category level (*Ours-per*) and the combination of all 6 categories (*Ours-all*).

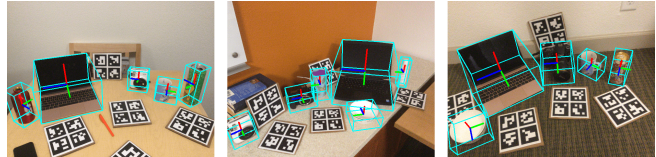
5.2. Comparison on novel objects with unknown 3D models

Dataset and baseline settings Two datasets are provided in [47] spanning 6 categories (*i.e.*, *bottle*, *bowl*, *camera*, *can*, *laptop*, *mug*). The REAL275 dataset has 8000 real-world RGB-D images from 18 different scenes and 42 objects, where 6 scenes including 18 objects are used for testing. Another dataset, CAMERA, is a synthetic dataset generated using CAD meshes from ShapeNet [5], whose training set includes 1085 meshes among the 6 categories.

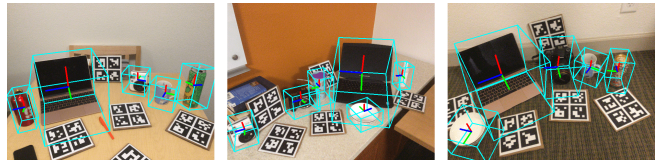
NOCS [47] and Tian *et al.* [43] train on both the synthetic (CAMERA) and real (REAL275) data and use the RGBD data for full pose estimation. Tian *et al.* also combine the depth map with RGB image for network input to regress the target correspondences for registration. In contrast, Chen *et al.* [8] train their neural analysis-by-synthesis approach for pose estimation only with the synthetic training objects from CAMERA, although the 2D segmentation backbone from [47] finetuned on REAL275 is used; further, they perform RGB-based rotation estimation and estimate translation with the depth data to reduce scale ambiguity.

We follow [8] to use the same 2D segmentation backbone, train our network only on the synthetic CAMERA dataset, and use depth to compute the object scale and translation after estimating the rotation from the RGB input. To establish the reference rotation set \mathcal{R} (Sec. 4), we employ K-means on the groundtruth rotations from the CAMERA training images to get 5000 samples. Following [8], we report the average precision (AP) on REAL275 regarding different thresholds of rotation and translation errors in Fig. 3.

Category level training We first train networks for each object category (denoted *Ours-per*) as is done by the previous works [47, 8, 43]. On average, we significantly outperform NOCS [47] and Chen *et al.* [8] in rotation estimation, especially when the error threshold is less than 30° . Meanwhile, our translation estimation is comparable with [47, 8]. Qualitative results are visualized in Fig. 4. Among the different categories, we perform better in the categories of bottle, can, and mug, where the rotation is determined mostly by the overall shape appearance. We note that the camera category becomes a bottleneck for our method, as it relies on subtle texture differences to distinguish vastly different



(a) Groundtruth



(b) Our estimation result

Figure 4: Qualitative results on REAL275 with estimated orientations shown as projected bounding boxes.

poses, *e.g.*, the front and back of a camera show very similar appearances with a flat lens in the front and a display in the back, and our compressed latent representation may fail to capture such subtle variances (see Fig. 4). Moreover, compared with the synthetic training set, REAL275 covers much more limited viewpoints concentrating on frontal views for the camera category (see the supplementary material for details); while models of NOCS [47] and Tian *et al.* [43] trained on the real data can utilize this limited distribution, our method trained only on the synthetic data has no access to that information.

Cross category training In contrast to the category specific design of [8, 43, 47], handling all 6 categories together does not require any structural changes to our framework, except that to learn the increased number of training objects within 50k iterations, we have modified d_s to 0.999. Under this setting, our method (*Ours-all* in Fig. 3) still outperforms [8] when the rotation error threshold is smaller than 23° and [47] with the rotation error threshold between 8° and 38° . However, the larger cross-category shape variances lead to lower performance when compared with our network trained on the per-category level (*Ours-per*).

5.3. Comparison on objects with known 3D models

Dataset and baseline settings T-LESS [19] contains 30 textureless industrial parts with very different shapes and symmetries (see the supplementary for visualization of object shapes). The CAD and reconstructed meshes are provided for all objects. Since the reconstructed meshes usu-

Method	Train respective networks		Train jointly on Obj 1-18	
	AAE[39, 40]	Pix2Pose[31]	Multipath-AAE[38]	Multipath-AAE[38] [†]
Ave. on Obj 1-18	62.57	29.5	51.75	60.75
Ave. on Obj 19-30	66.63	29.5	52.49	59.89
Ave. on Obj 1-30	64.19	29.5	52.04	60.41
				66.43

Table 1: Comparison on all test instances whose visible portion $>10\%$ in TLESS Primesense images. Pose estimations are performed based on the 2D GT bounding boxes, while [†] indicates using 2D GT mask. Reported are the average recall rates with $e_{VSD} < 0.3$.

Method	Train respective networks for Obj 1-30			Train jointly on Obj 1-18	
	AAE [39, 40] +RetinaNet[27]	Pix2Pose [31] +RetinaNet[27]	EEGP-AAE [48] +RetinaNet[27]	Multipath-AAE[38] +MaskR-CNN[14]	Ours +RetinaNet[27]
Ave. on Obj 1-30	26.79	29.5	34.67	23.51	32.76

Table 2: Comparison of the full 2D detection and pose estimation pipeline on TLESS Primesense images. Reported are the average recall rates with $e_{VSD} < 0.3$.

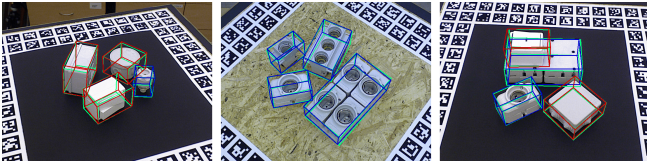


Figure 5: Qualitative results on T-LESS. Blue and red boxes respectively indicate our estimation on trained objects and unseen objects, while the green boxes indicate the groundtruth 6D pose.

ally have inaccurate 3D bounding boxes, which affects the RGB-based translation estimation, we report the performances of all methods by training and testing with the CAD meshes for fair comparison.

Unlike most of the instance-level methods [39, 40, 48, 31] that train specialized networks for each model, we follow Multipath-AAE [38] to train on the first 18 objects only and test on all 30 objects. Same as [39, 40, 38, 48], we build the reference rotation set \mathcal{R} with 92232 rotations from the combination of 36 in-plane rotations and 2562 equidistant spherical views sampled via [17]. Following [20], we use the visible surface discrepancy metric e_{VSD} with distance tolerance $20mm$ that is invariant to symmetry ambiguity, and report the recall rate at $e_{VSD} < 0.3$ for instances with visible portion $>10\%$ of all test images for 30 objects.

Results and discussions We first evaluate different methods with the groundtruth 2D bounding box, thus eliminating the inaccuracy brought by the 2D detection backbone. The results are reported in Tab. 1. Note that for the first 18 meshes on which all methods are trained, our result outperforms AAE [39, 40] and Multipath-AAE [38] by significant margins (*i.e.*, 5% for AAE, and around 7% for Multipath-AAE), even though AAE trains for each object a specific autoencoder, and Multipath-AAE assigns separate decoders for the 18 objects and optionally uses the groundtruth mask to eliminate the background noise for a better performance. In addition, our method generalizes better than Multipath-AAE to the novel objects (*i.e.*, Obj 19-30) with a 4% increase in the average recall rate.

We then adopt the RetinaNet [27] used in Pix2Pose [31] and EEGP-AAE [48] as the 2D detection backbone. Under the single object single instance protocol as described in [20], we compare with other RGB-based works [38, 31, 39, 40, 48], and report their average recall rates on all 30 objects in Tab. 2, with qualitative cases shown in Fig. 5 and per-object recall rates in supplementary materials. Note that not only do we outperform Multipath-AAE for over 9%, but also we gain comparable or even better performances than instance-level methods that train specific networks for each of the 30 objects.

5.4. Ablation study

In this section, we validate our designs of the shape conditioned pose code generation and metric learning for object shapes with ablation tests. We use two experimental settings from the last section for demonstration: one is to train our network on the first 18 objects of T-LESS [19], and the other is to train the network on the combination of 6 categories from CAMERA [47].

Shape conditioned pose code generation We first discuss the necessity to generate pose codes conditioned on their shape codes, by separating the shape codes from the pose codebook generation. To this end, we modify Eq. 4 by replacing the bilinear map \mathbf{W} with a multi-layer perceptron MLP and using only the HSH encoding as input, *i.e.* $\text{MLP}(FC(\mathbf{h}_p))$. The MLP has four layers of width [1024, 1024, 1024, 128] and thus more trainable weights than \mathbf{W} . The mean average precision on REAL275 reported in Tab. 3 (2nd, 4th rows) shows that the performance significantly degrades when the shape code is separated from pose code generation, indicating the difficulty of learning independent latent representations of shape and pose.

To further visualize the effectiveness of the pose code generation, given an object o , we inspect the relationship between two sets of latent pose representations, $\mathcal{C}_E^P = \{z_p\}_{p \in \mathcal{R}}$ generated by the encoder E and $\mathcal{C}_B^P = \{z_{o,p}\}_{p \in \mathcal{R}}$ by the conditioned block B , where \mathcal{R} contains 8020 rotations from 401 quasi-equidistant views sampled by [11] combined with 20 in-plane rotations. Ideally, the two sets of latent codes should coincide with each other, so that the conditionally generated pose codebook can be effective for rotation estimation.

To check if this is true, we apply principal component analysis (PCA) respectively to $\mathcal{C}_E^P, \mathcal{C}_B^P$, and visualize the top three principal components. As shown in Fig. 6 where we use a box-like mesh (Obj-6) and a cylinder-like mesh (Obj-17) from the T-LESS training set, we observe that our entanglement of shape and pose information enables \mathcal{C}_B^P to well synchronize with \mathcal{C}_E^P for objects with different degrees of symmetry, though for Obj-6 a global rotation of the principal component projections between \mathcal{C}_B^P and \mathcal{C}_E^P exists due to the nearly isotropic distribution of latent codes. On the contrary, when the shape encoding is isolated from generating

Pose code generation	AP_5	AP_{10}	AP_{15}	AP_{20}	AP_{30}	AP_{60}
MLP($FC(\mathbf{h}_p)$)	3.4	12.2	25.8	34.7	46.6	67.9
MLP($FC(\text{sg}(\mathbf{c}_o)), FC(\mathbf{h}_p)$)	10.3	28.1	44.1	54.0	65.6	72.9
W ($FC(\text{sg}(\mathbf{c}_o)), FC(\mathbf{h}_p)$)	7.5	28.7	48.4	60.2	70.9	77.4

Table 3: Ablation study on the design of shape conditioned pose code generation. Reported are the mean average precisions at different thresholds of rotation error (*i.e.*, 5° , 10° , 15° , 20° , 30° , 60°) on 6 categories of REAL275.

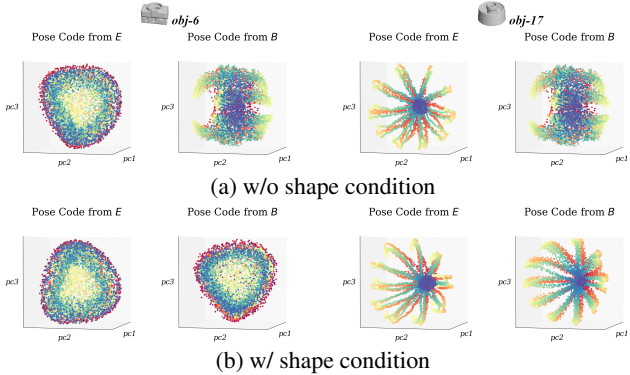


Figure 6: Visualization of the top three principal component projections ($pc1$, $pc2$, $pc3$) for two sets of latent pose codes \mathcal{C}_E^P from E and \mathcal{C}_B^P from B on two T-LESS objects. The point color encodes a unique rotation in \mathcal{R} sampled as a list of viewpoints starting from the north pole and ending on the south pole, with the list index linearly mapped to the color spectrum (blue \rightarrow green \rightarrow red). The shape conditioned pose codes (b) well capture the symmetries of different objects, while unconditioned pose codes (a) fails.

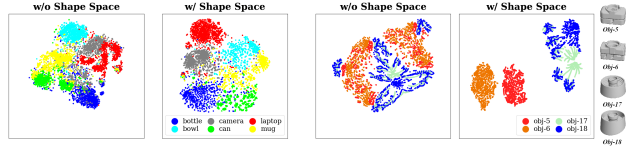
the pose codebook, it becomes difficult for \mathcal{C}_B^P to follow the pattern of \mathcal{C}_E^P for different objects. Such contrast demonstrates the necessity of entangling the shape information for the pose code generation.

Given the necessity to generate shape conditioned pose code, we move on to validate the design of how to combine pose and shape information. Instead of the bilinear tensor product entanglement adopted by our pipeline, an intuitive idea is to simply concatenate the shape and pose rotational encoding and process by an MLP, *i.e.* MLP($FC(\text{sg}(\mathbf{c}_o)), FC(\mathbf{h}_p)$) where MLP has four layers of width [1024, 1024, 1024, 128] and thus a larger number of trainable weights than the bilinear map. The comparison on REAL275 in Tab. 3 (3rd, 4th rows) shows that the bilinear map outperforms MLP for rotation error thresholds $>10^\circ$; the better performance of MLP at 5° may be attributed to its powerful overfitting capacity that however does not generalize to a wider range.

Contrastive metric learning of latent shape space Finally, we validate if the contrastive metric learning of the latent shape encoding is helpful. To this end, we remove the shape space metric loss L_{shape} , and use \mathbf{z}_o instead of $\text{sg}(\mathbf{c}_o)$ in Eq. 4 for conditioning the pose code generation. The mean average precision reported in Tab. 4 shows

	AP_5	AP_{10}	AP_{15}	AP_{20}	AP_{30}	AP_{60}
w/o shape space	2.8	13.4	30.1	43.4	60.1	76.0
w/ shape space	7.5	28.7	48.4	60.2	70.9	77.4

Table 4: Ablation study on the contrastive metric learning for object shape space. Reported are the mean average precisions at different thresholds of rotation error (*i.e.*, 5° , 10° , 15° , 20° , 30° , 60°) on 6 categories of REAL275.



(a) CAMERA objects

(b) T-LESS objects

Figure 7: tSNE visualization of \mathbf{z}_o of training images of 6 CAMERA categories and 4 T-LESS objects, respectively. With shape space metric learning the better regularity on shape latent space is observed.

our shape space metric learning enables significant performance improvement and thus better generalization to unseen objects. We also visualize the latent shape space \mathbf{z}_o with tSNE in Fig. 7, for 1,000 samples per category from the CAMERA training data, and 1,000 samples per object for 4 T-LESS objects. With the shape space metric learning, we observe much better intra-category clustering and inter-category separation, especially on categories such as the laptop and camera, though we have not explicitly constrained the category-level classification. On the 4 T-LESS objects, the introduction of shape prior not only well separates the box-like meshes (Obj-5,6) from the cylinder-like meshes (Obj-17,18), but also recognizes the detailed geometric differences between Obj-5 and Obj-6; in comparison, the shape codes for different objects are mixed together when the shape space metric learning is removed.

6. Conclusion

We have presented a scalable approach for estimating the 6D poses of multiple objects, allowing the generalization to objects unseen during training. Noticing that the key to scalability is to leverage the similarities of object shapes, we train an auto-encoder to disentangle the implicit representations of an observed object view into the shape code and the pose code, such that a metric space for the shape representation even across categories can be learned, and the pose code can be compared with canonical rotations for pose estimation. Due to the different symmetries of objects, the disentanglement into independent shape and pose spaces is fundamentally difficult, which we resolve by making the pose codebook generation dependent on the shape code. We demonstrated the efficiency of our framework by testing it on two commonly used benchmarks that involve either known or unknown 3D models at test time, where we obtain results that compare favorably to the respective state of the arts. We have also validated the key designs by ablation tests, showing that the disentanglement and

re-entanglement by our approach indeed captures object-specific symmetries, and the shape space metric learning helps generalization.

References

- [1] Yoshua Bengio, Aaron Courville, and Pascal Vincent. Representation learning: A review and new perspectives. *IEEE Transactions on Pattern Analysis and Machine Intelligence*, 35(8), 2013. [3](#)
- [2] Gideon Billings and Matthew Johnson-Roberson. Silhonet: An rgb method for 3d object pose estimation and grasp planning. *arXiv preprint arXiv:1809.06893*, 2018. [2](#)
- [3] Diane Bouchacourt, Mark Ibrahim, and Stéphane Deny. Addressing the topological defects of disentanglement via distributed operators, 2021. [2](#), [3](#)
- [4] Eric Brachmann, Frank Michel, Alexander Krull, Michael Ying Yang, Stefan Gumhold, et al. Uncertainty-driven 6d pose estimation of objects and scenes from a single rgb image. In *Proceedings of the IEEE Conference on Computer Vision and Pattern Recognition*, pages 3364–3372, 2016. [2](#)
- [5] Angel X. Chang, Thomas Funkhouser, Leonidas Guibas, Pat Hanrahan, Qixing Huang, Zimo Li, Silvio Savarese, Manolis Savva, Shuran Song, Hao Su, Jianxiong Xiao, Li Yi, and Fisher Yu. Shapenet: An information-rich 3d model repository, 2015. [2](#), [6](#)
- [6] Dengsheng Chen, Jun Li, Zheng Wang, and Kai Xu. Learning canonical shape space for category-level 6d object pose and size estimation. In *Proceedings of the IEEE/CVF Conference on Computer Vision and Pattern Recognition (CVPR)*, June 2020. [2](#)
- [7] Ting Chen, Simon Kornblith, Mohammad Norouzi, and Geoffrey Hinton. A simple framework for contrastive learning of visual representations. In *International conference on machine learning*, pages 1597–1607. PMLR, 2020. [3](#)
- [8] Xu Chen, Zijian Dong, Jie Song, Andreas Geiger, and Otmar Hilliges. Category level object pose estimation via neural analysis-by-synthesis. In *European Conference on Computer Vision (ECCV)*, 2020. [1](#), [2](#), [3](#), [5](#), [6](#)
- [9] Xi Chen, Yan Duan, Rein Houthoofd, John Schulman, Ilya Sutskever, and Pieter Abbeel. Infogan: Interpretable representation learning by information maximizing generative adversarial nets. In *Advances in Neural Information Processing Systems 29*, pages 2172–2180. 2016. [3](#)
- [10] Vincent Dumoulin, Ethan Perez, Nathan Schucher, Florian Strub, Harm de Vries, Aaron Courville, and Yoshua Bengio. Feature-wise transformations. *Distill*, 3(7):e11, 2018. [3](#), [4](#)
- [11] Álvaro González. Measurement of areas on a sphere using fibonacci and latitude–longitude lattices. *Mathematical Geosciences*, 42(1):49, 2010. [7](#)
- [12] Alexander Grabner, Peter M Roth, and Vincent Lepetit. Location field descriptors: Single image 3d model retrieval in the wild. In *2019 International Conference on 3D Vision (3DV)*, pages 583–593. IEEE, 2019. [2](#)
- [13] Kaiming He, Haoqi Fan, Yuxin Wu, Saining Xie, and Ross Girshick. Momentum contrast for unsupervised visual representation learning. In *Proceedings of the IEEE Conference on Computer Vision and Pattern Recognition (CVPR)*, 2020. [3](#)
- [14] Kaiming He, Georgia Gkioxari, Piotr Dollár, and Ross Girshick. Mask r-cnn. In *Proceedings of the IEEE International Conference on Computer Vision (ICCV)*, pages 2961–2969, 2017. [7](#)
- [15] Irina Higgins, David Amos, David Pfau, Sebastien Racaniere, Loic Matthey, Danilo Rezende, and Alexander Lerchner. Towards a definition of disentangled representations. *arXiv preprint arXiv:1812.02230*, 2018. [3](#)
- [16] Irina Higgins, Loic Matthey, Arka Pal, Christopher Burgess, Xavier Glorot, Matthew Botvinick, Shakir Mohamed, and Alexander Lerchner. beta-vae: Learning basic visual concepts with a constrained variational framework. In *ICLR*, 2017. [3](#)
- [17] Stefan Hinterstoisser, Selim Benhimane, Vincent Lepetit, Pascal Fua, and Nassir Navab. Simultaneous recognition and homography extraction of local patches with a simple linear classifier. In *BMVC*, pages 1–10, 2008. [7](#)
- [18] Stefan Hinterstoisser, Vincent Lepetit, Slobodan Ilic, Stefan Holzer, Gary Bradski, Kurt Konolige, and Nassir Navab. Model based training, detection and pose estimation of texture-less 3d objects in heavily cluttered scenes. In *Asian conference on computer vision*, pages 548–562. Springer, 2012. [2](#)
- [19] Tomáš Hodaň, Pavel Haluza, Štěpán Obdržálek, Jiří Matas, Manolis Lourakis, and Xenophon Zabulis. T-LESS: An RGB-D dataset for 6D pose estimation of texture-less objects. *IEEE Winter Conference on Applications of Computer Vision (WACV)*, 2017. [2](#), [5](#), [6](#), [7](#)
- [20] Tomas Hodan, Frank Michel, Eric Brachmann, Wadim Kehl, Anders GlentBuch, Dirk Kraft, Bertram Drost, Joel Vidal, Stephan Ihrke, Xenophon Zabulis, et al. Bop: Benchmark for 6d object pose estimation. In *Proceedings of the European Conference on Computer Vision (ECCV)*, pages 19–34, 2018. [7](#)

- [21] Tero Karras, Samuli Laine, and Timo Aila. A style-based generator architecture for generative adversarial networks. In *Proceedings of the IEEE/CVF Conference on Computer Vision and Pattern Recognition*, pages 4401–4410, 2019. [3](#)
- [22] Tero Karras, Samuli Laine, Miika Aittala, Janne Hellsten, Jaakko Lehtinen, and Timo Aila. Analyzing and improving the image quality of stylegan. In *Proceedings of the IEEE/CVF Conference on Computer Vision and Pattern Recognition*, pages 8110–8119, 2020. [3](#)
- [23] Wadim Kehl, Fabian Manhardt, Federico Tombari, Slobodan Ilic, and Nassir Navab. Ssd-6d: Making rgb-based 3d detection and 6d pose estimation great again. In *Proceedings of the IEEE International Conference on Computer Vision*, pages 1521–1529, 2017. [1](#), [2](#)
- [24] Ilyes Khemakhem, Diederik Kingma, Ricardo Monti, and Aapo Hyvarinen. Variational autoencoders and nonlinear ica: A unifying framework. In *Proceedings of International Conference on Artificial Intelligence and Statistics*, volume 108 of *Proceedings of Machine Learning Research*. PMLR, 2020. [3](#)
- [25] Diederik P Kingma and Jimmy Ba. Adam: A method for stochastic optimization. *arXiv preprint arXiv:1412.6980*, 2014. [5](#)
- [26] Vincent Lepetit. Recent advances in 3d object and hand pose estimation. *arXiv preprint arXiv:2006.05927*, 2020. [2](#)
- [27] Tsung-Yi Lin, Priya Goyal, Ross Girshick, Kaiming He, and Piotr Dollár. Focal loss for dense object detection. In *Proceedings of the IEEE international conference on computer vision*, pages 2980–2988, 2017. [7](#)
- [28] Francesco Locatello, Gabriele Abbati, Thomas Rainforth, Stefan Bauer, Bernhard Schölkopf, and Olivier Bachem. On the fairness of disentangled representations. In *Advances in Neural Information Processing Systems*, volume 32. Curran Associates, Inc., 2019. [3](#)
- [29] Francesco Locatello, Stefan Bauer, Mario Lucic, Gunnar Raetsch, Sylvain Gelly, Bernhard Schölkopf, and Olivier Bachem. Challenging common assumptions in the unsupervised learning of disentangled representations. In Kamalika Chaudhuri and Ruslan Salakhutdinov, editors, *Proceedings of International Conference on Machine Learning*, volume 97 of *Proceedings of Machine Learning Research*. PMLR, 2019. [3](#)
- [30] John Martyn, Guifre Vidal, Chase Roberts, and Stefan Leichenauer. Entanglement and tensor networks for supervised image classification, 2020. [4](#)
- [31] Kiru Park, Timothy Patten, and Markus Vincze. Pix2pose: Pixel-wise coordinate regression of objects for 6d pose estimation. *arXiv preprint arXiv:1908.07433*, 2019. [2](#), [7](#)
- [32] A. Pasha Hosseinbor, Moo K. Chung, Cheng Guan Koay, Stacey M. Schaefer, Carien M. van Reekum, Lara Peschke Schmitz, Matt Sutterer, Andrew L. Alexander, and Richard J. Davidson. 4d hyperspherical harmonic (hyperspharm) representation of surface anatomy: A holistic treatment of multiple disconnected anatomical structures. *Medical Image Analysis*, 22(1):89–101, 2015. [4](#)
- [33] Sida Peng, Yuan Liu, Qixing Huang, Xiaowei Zhou, and Hujun Bao. Pvnnet: Pixel-wise voting network for 6dof pose estimation. In *Proceedings of the IEEE Conference on Computer Vision and Pattern Recognition*, pages 4561–4570, 2019. [2](#)
- [34] Giorgia Pitteri, Aurélie Bugeau, Slobodan Ilic, and Vincent Lepetit. 3D Object Detection and Pose Estimation of Unseen Objects in Color Images with Local Surface Embeddings. In *15th Asian Conference on Computer Vision*, Kyoto (virtual conference), Japan, Nov. 2020. [2](#), [5](#)
- [35] Emmanouil Antonios Platanios, Mrinmaya Sachan, Graham Neubig, and Tom Mitchell. Contextual parameter generation for universal neural machine translation. In *Proceedings of the 2018 Conference on Empirical Methods in Natural Language Processing*, pages 425–435, 2018. [4](#)
- [36] Mahdi Rad and Vincent Lepetit. Bb8: A scalable, accurate, robust to partial occlusion method for predicting the 3d poses of challenging objects without using depth. In *Proceedings of the IEEE International Conference on Computer Vision*, pages 3828–3836, 2017. [1](#), [2](#)
- [37] Szymon Rusinkiewicz. A symmetric objective function for icp. *ACM Trans. Graph.*, 38(4), July 2019. [5](#)
- [38] Martin Sundermeyer, Maximilian Durner, En Yen Puang, Zoltan-Csaba Marton, Narunas Vaskevicius, Kai O Arras, and Rudolph Triebel. Multi-path learning for object pose estimation across domains. In *Proceedings of the IEEE Conference on Computer Vision and Pattern Recognition*, pages 13916–13925, 2020. [1](#), [2](#), [3](#), [5](#), [7](#)
- [39] Martin Sundermeyer, Zoltan-Csaba Marton, Maximilian Durner, Manuel Brucker, and Rudolph Triebel. Implicit 3d orientation learning for 6d object detection from rgb images. In *Proceedings of the European Conference on Computer Vision (ECCV)*, pages 699–715, 2018. [2](#), [3](#), [7](#)
- [40] Martin Sundermeyer, Zoltan-Csaba Marton, Maximilian Durner, and Rudolph Triebel. Augmented autoencoders: Implicit 3d orientation learning for 6d object

- detection. *International Journal of Computer Vision*, pages 1–16, 2019. 2, 5, 7
- [41] Bugra Tekin, Sudipta N Sinha, and Pascal Fua. Real-time seamless single shot 6d object pose prediction. In *Proceedings of the IEEE Conference on Computer Vision and Pattern Recognition*, pages 292–301, 2018. 2
- [42] Joshua B. Tenenbaum and William T. Freeman. Separating style and content with bilinear models. *Neural Computation*, 12(6):1247–1283, 2000. 4
- [43] Meng Tian, Marcelo H Ang Jr, and Gim Hee Lee. Shape prior deformation for categorical 6d object pose and size estimation. In *Proceedings of the European Conference on Computer Vision (ECCV)*, August 2020. 1, 2, 3, 5, 6
- [44] Zhi Tian, Chunhua Shen, and Hao Chen. Conditional convolutions for instance segmentation. In *Proc. Eur. Conf. Computer Vision (ECCV)*, 2020. 4
- [45] Aaron van den Oord, Yazhe Li, and Oriol Vinyals. Representation learning with contrastive predictive coding. *arXiv preprint arXiv:1807.03748*, 2018. 3
- [46] Ashish Vaswani, Noam Shazeer, Niki Parmar, Jakob Uszkoreit, Llion Jones, Aidan N Gomez, Łukasz Kaiser, and Illia Polosukhin. Attention is all you need. In *Advances in Neural Information Processing Systems*, volume 30. Curran Associates, Inc., 2017. 4
- [47] He Wang, Srinath Sridhar, Jingwei Huang, Julien Valentin, Shuran Song, and Leonidas J Guibas. Normalized object coordinate space for category-level 6d object pose and size estimation. In *Proceedings of the IEEE Conference on Computer Vision and Pattern Recognition*, pages 2642–2651, 2019. 1, 2, 5, 6, 7
- [48] Yilin Wen, Hao Pan, Lei Yang, and Wenping Wang. Edge enhanced implicit orientation learning with geometric prior for 6d pose estimation. *IEEE Robotics and Automation Letters (IROS)*, 5(3), 2020. 2, 3, 7
- [49] Zhirong Wu, Yuanjun Xiong, Stella X Yu, and Dahua Lin. Unsupervised feature learning via non-parametric instance discrimination. In *Proceedings of the IEEE Conference on Computer Vision and Pattern Recognition (CVPR)*, pages 3733–3742, 2018. 3
- [50] Yu Xiang, Tanner Schmidt, Venkatraman Narayanan, and Dieter Fox. Posecnn: A convolutional neural network for 6d object pose estimation in cluttered scenes. *arXiv preprint arXiv:1711.00199*, 2017. 1, 2
- [51] Haoruo Zhang and Qixin Cao. Detect in rgb, optimize in edge: Accurate 6d pose estimation for texture-less industrial parts. In *2019 International Conference on Robotics and Automation (ICRA)*, pages 3486–3492. IEEE, 2019. 2
- [52] Lin Zhao. Spherical and spheroidal harmonics: Examples and computations, 2017. 4